

UNIVERSITY OF CAMBRIDGE  
DEPARTMENT OF ENGINEERING

MASTERS PROJECT REPORT



# Propulsion Systems for [small?] VTOL Electric Vehicles

Jordan Sandberg Eriksen

SUPERVISED BY: Dr Sam Grimshaw

## Abstract

Abstract here..

## Contents

<b>1</b>	<b>Introduction</b>	<b>1</b>
1.1	Literature Review . . . . .	1
1.2	Research Questions . . . . .	1
1.3	Approach . . . . .	1
<b>2</b>	<b>Flying Test Bed and Propulsor Design</b>	<b>1</b>
2.1	System Design . . . . .	1
2.1.1	Flying vehicle development . . . . .	1
2.1.2	Subsystem Functions . . . . .	3
2.1.3	Subsystem Interaction . . . . .	4
2.1.4	Telemetry . . . . .	4
2.2	Aerodynamic Design . . . . .	5
2.2.1	Figure of Merit and Design Point . . . . .	5
2.2.2	Mid-line Blade Design . . . . .	8
2.2.3	3D Blade Design . . . . .	14
2.3	Electrical Design . . . . .	23
2.3.1	Motor Requirements . . . . .	23
2.3.2	Choice of Electric Motor . . . . .	23
2.3.3	Power Supply . . . . .	23
2.3.4	Instrumentation Design . . . . .	23
2.4	Mechanical Design . . . . .	24
2.4.1	Propulsor Dimensions . . . . .	24
2.4.2	Shroud Tip Clearance . . . . .	24
2.4.3	Hollow Stators . . . . .	24
2.4.4	3D Printing . . . . .	24
<b>3</b>	<b>Methods</b>	<b>25</b>
3.1	Experiments . . . . .	25
3.1.1	Stationary Propulsor Test . . . . .	25
3.1.2	Flying Test Bed . . . . .	25
3.2	Experimental Method & Data Processing . . . . .	25
3.2.1	Non-dimensional Quantities . . . . .	25
3.2.2	Instrumentation . . . . .	25
3.2.3	Data Acquisition . . . . .	25
3.2.4	Flight Management for Auto Position Hold . . . . .	25
3.2.5	Cage Design & Tether . . . . .	25

<b>4</b>	<b>Experimental Results</b>	<b>25</b>
4.1	Stationary Propulsor Test . . . . .	25
4.1.1	Comparison of Vortex Distributions . . . . .	25
4.1.2	Version 1.0 EDF . . . . .	25
4.1.3	Version 2.0 EDF . . . . .	26
4.1.4	Version 3.0 EDF . . . . .	26
4.1.5	Propeller . . . . .	26
4.2	Hover Tests . . . . .	26
4.2.1	Propeller Performance . . . . .	26
4.2.2	Hover Test Limitations . . . . .	26
<b>5</b>	<b>Future Work</b>	<b>26</b>
5.1	Propulsor Design . . . . .	27
5.1.1	Stationary Propulsor Tests . . . . .	27
5.1.2	Contra-rotating Ducted Fan . . . . .	27
5.1.3	Computational Fluid Dynamics . . . . .	27
5.2	Flying Test Bed Experiments . . . . .	27
<b>6</b>	<b>Conclusions</b>	<b>27</b>

Electric Vertical Take-Off and Landing	e-VTOL		
Flying Test-Bed	FTB		
Axial Flow Velocity	$V_x$		
Fan Speed	$\Omega$		
Fan Hub Radius	$r_h$		
Fan Casing Radius	$r_c$		
Fan Mid-line Radius	$r_m$		
Mid-line Fan Speed	$U$	$= \Omega \cdot r_m$	
Flow Coefficient	$\phi$	$= \frac{V_x}{U}$	
Stage Loading	$\psi$	$= \frac{\Delta h_0}{U^2}$	

# Nomenclature

e-VTOL Test  
FTB Test  
 $V_x$  Axial flow velocity  
 $\Omega$   
 $r_h$   
 $r_c$   
 $r_m$   
 $U$   
 $\phi$  Flow coefficient  
 $\psi$  Stage loading

## Introduction

Intro and motivation

Consider Heilmeier when structuring this section.

- Integrate battery into casing, increase payload volume/utilise space

### 1.1 Literature Review

### 1.2 Research Questions

### 1.3 Approach

High level overview of what's been done and how the report is set out.

## Flying Test Bed and Propulsor Design

### 2.1 System Design

#### 2.1.1 Flying vehicle development

A UROP was conducted in the summer preceding this project during which an axi-symmetric quadcopter flying test bed was designed and tested. The two challenges addressed were structural design of the chassis, and the customisation of flight control hardware and software. The UROP concluded with successful hover testing of the flying test bed. Off-the-shelf 10in. propellers were used in the test<sup>1</sup>.

#### Mechanical design

The test bed was designed to be rapidly 3D printable, light weight – whilst maintaining

---

<sup>1</sup>REFERENCE UROP REPORT

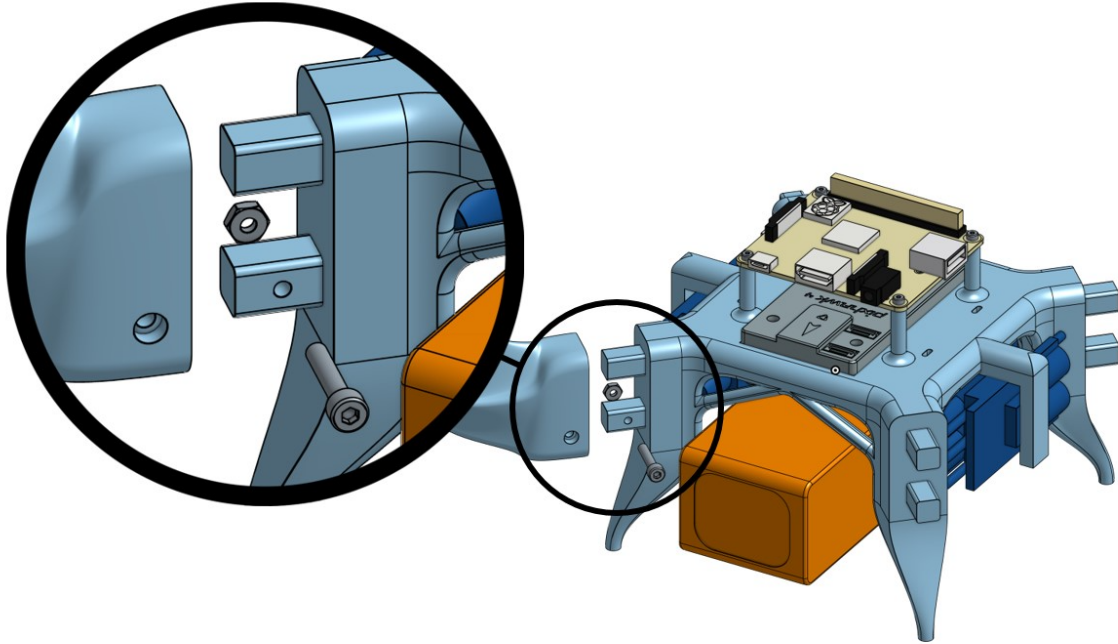


Figure 1: Flying test bed chassis showing exploded detail of double mortise and tenon joint for propulsor arms

structural integrity – and modular to allow various propulsors and instrumentation to be mounted. Instrumentation management and flight hardware are mounted on a central chassis that is 3D printed as one piece for rigidity and to reduce complexity. Cantilevered propulsor arms are attached to the central chassis with a double mortise and tenon style mount, fastened by one M3 cap-head as in Fig. 1. Modularity allows for design iteration and rapid part replacement if required.

The following hardware is mounted directly onto the central chassis:

- ***Pixhawk* 4 Flight Control hardware** – Packaged, customizable autopilot hardware
- **PM07 Power Module** – Power module managing distribution of power from battery/power supply to flight controllers, other on-board computers, and motors
- **Raspberry Pi 3 Model A+** – On-board computer managing data acquisition and assisting flight controller automation
- **ADCPi ADC Breakout** – Analogue to digital converter mounted directly to the Raspberry Pi 3
- **4x Aerostar 50A ESC** – Electronic Speed Controller driving BLDCM motors
- **Optional: Turnigy 5000mAh 14.8V (4-cell) Battery** – Large capacity 14.8V (nominal) battery. Can be replaced by a tethered 12V power supply.

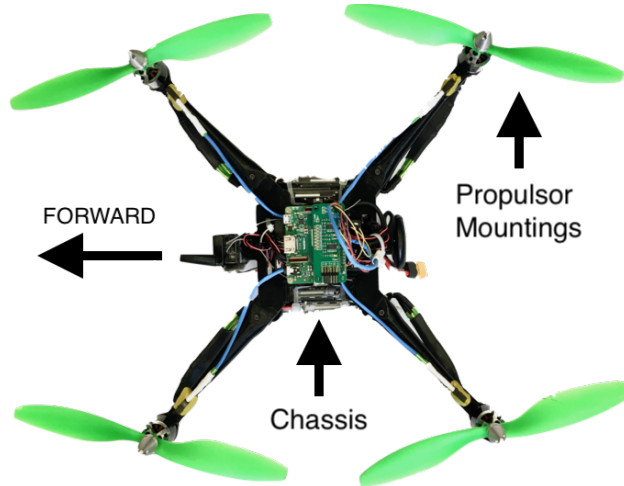


Figure 2: Image of flying test bed with propellers attached

The central chassis has dimensions of approximately  $125mm \times 139mm \times 93mm$  (see Fig. 13). It has a dry mass (excluding battery) of  $0.529kg$  and the battery has a mass of  $0.466kg$ .

#### Customisation of *Pixhawk 4* flight hardware/software

Pixhawk 4 is a packaged flight control hardware system running open source PX4 firmware. Interaction with the system is via the GUI QGroundControl and either a wireless telemetry transmitter-receiver pair or a serial connection (such as a USB). QGroundControl allows a predetermined automated flight path to be followed or alternatively the hardware can be configured to allow manual control provided adequate control inputs can be provided (a 16-channel remote with an 8-channel PPM-PWM converter is used here). The PM4 firmware includes various airframe configuration profiles, enabling it to adapt to the vehicle configuration and motor layout. The flying test bed is configured as a symmetric 'X' quadcopter. The profile was tuned to the flying test bed by varying PID gains on the control software, ensuring stable operation in hover. It provides a stable hover mode that is intended to reduce horizontal position deviation and maintain a fixed altitude. This means only small corrective inputs are required from the operator to ensure near stationary hover even in enclosed environments. It was found however that wall effects can be significant and so care must be taken when operating in such environments.

#### 2.1.2 Subsystem Functions

##### Raspberry Pi 3 Model A+ (RPi3)

The RPi3 is a light-weight, small-footprint, 64-bit quad-core processor with UNIX-based operating system and Wi-Fi connectivity that can be run 'blind' through an SSH connection from a remote machine. It provides data acquisition and on-board data processing in Python and is used to pre-process test data before wirelessly transferring it back to the

remote machine. RPi3 has 28 general purpose input/output (GPIO) pins as well as I<sup>2</sup>C and serial interfaces among others.

### **ADCPi ADC Breakout**

The ADC breakout board is designed specifically for the RPi3. Operating through the I<sup>2</sup>C interface, each breakout board provides an 8-channel ADC at 11 to 17 bit resolution with sample rates of 240 to 3.75 *samples/sec* respectively.

### **PM07 Power Module**

Designed to operate in tandem with the Pixhawk 4 flight controller, the PM07 provides power control for all the high-power outputs (such as the motors) as well as a regulated 5V output for the flight controller and RPi3. Power input is 7-51V DC and the output current is limited to 120A (approximately 30A per propulsor). The battery selected can operate up to 125A to accommodate this demand. PM07 also provides 2 ADC inputs.

#### **2.1.3 Subsystem Interaction**

Pixhawk 4 provides simple subsystem interaction through its input ports. 5 ports connect the flight controller to the power module: 2x power inputs, 1x motor PWM outputs, 1x auxiliary PWM output, and 1x ADC input. The serial port on the Pixhawk 4 is rewired to connect to the RPi3's UART TXD and RXD terminals (Fig.12 shows all connections made to the RPi3 header). The I<sup>2</sup>C port connects to an I<sup>2</sup>C bus that allows up to 5 devices to interface with the Pixhawk 4, including 3 ultrasound sensors measuring proximity in the x, y, and z directions. These sensors can optionally be connected via the ADC for use by the RPi3. Figure 3 shows schematically how the subsystems interact.

#### **2.1.4 Telemetry**

##### **Pixhawk 4 wireless telemetry**

The plug-and-play telemetry module allows wireless connection to the Pixhawk 4 from a ground control station on a remote machine such as QGroundControl. This is used to communicate with the Pixhawk 4 about flight control and to log power usage data (PM07 voltage and current output).

##### **SSH/SCP on RPi3**

RPi3 is wireless enabled allowing it to be accessed remotely via the SSH (secure shell) protocol. SCP (secure copy protocol) allows files to be copied to and from the RPi3. This is used after data collection to collect all data on the remote machine. A dedicated wireless router is used to connect the RPi3 to a remote machine – done automatically on start-up of the RPi3.



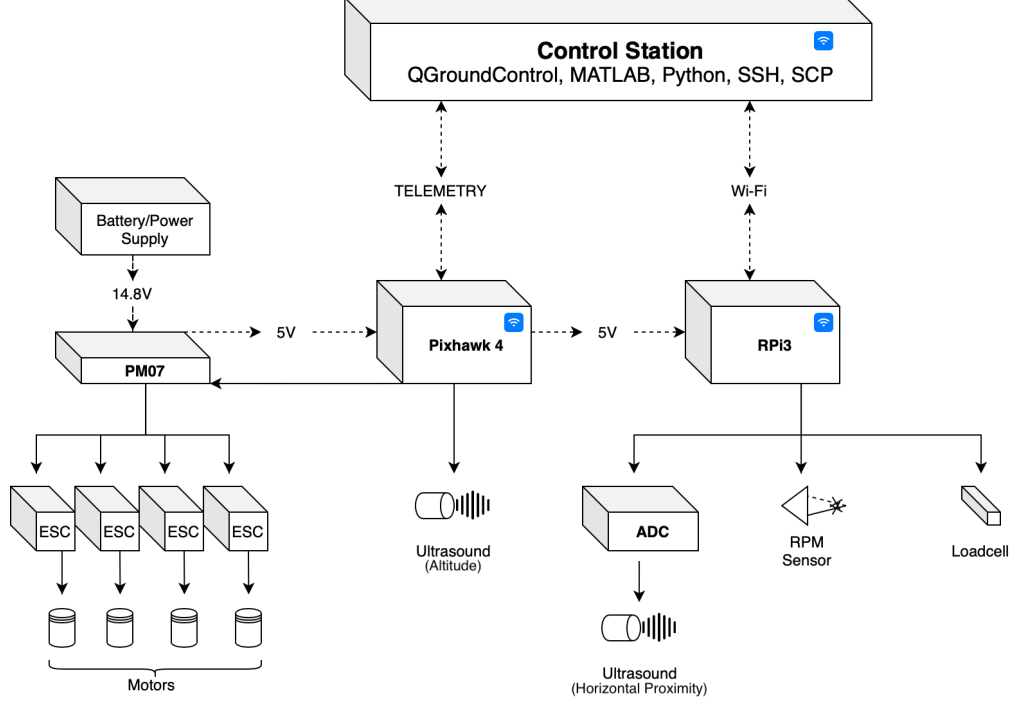


Figure 3: Subsystem schematic of flying test bed

## 2.2 Aerodynamic Design

The aerodynamic design of an electric ducted fan, 3D printed in PLA, is described below. The flying test bed is powered by 4 ducted fans and is required to be able to achieve a steady hover with a payload equal to the weight of the flying test bed chassis. Figure 4 shows an overview of the ducted fan configuration with design variables labelled where appropriate.

### 2.2.1 Figure of Merit and Design Point

A low-speed (incompressible) ducted fan in hover fundamentally differs from both a propeller and a ducted fan in high-speed free stream velocity. A propeller's exit static pressure is approximately equal to atmospheric, however a low-speed ducted fan can vary its exit pressure by varying the area ratio,  $\sigma$ , defined as the ratio of exit flow area ( $A_e$ ) and blade passage flow area ( $A_x$ ), as in Eqn. 1.

$$\sigma = \frac{A_e}{A_x} \quad (1)$$

As the exit static pressure must be approximately atmospheric, assuming the diffuser flow remains attached variation in  $\sigma$  will result in a variation in  $p_x$ , the blade passage static pressure.

A ducted fan in non-zero free stream velocity is required to reduce frontal area in order to decrease aerodynamic drag, however a ducted fan in static hover is not. This means the

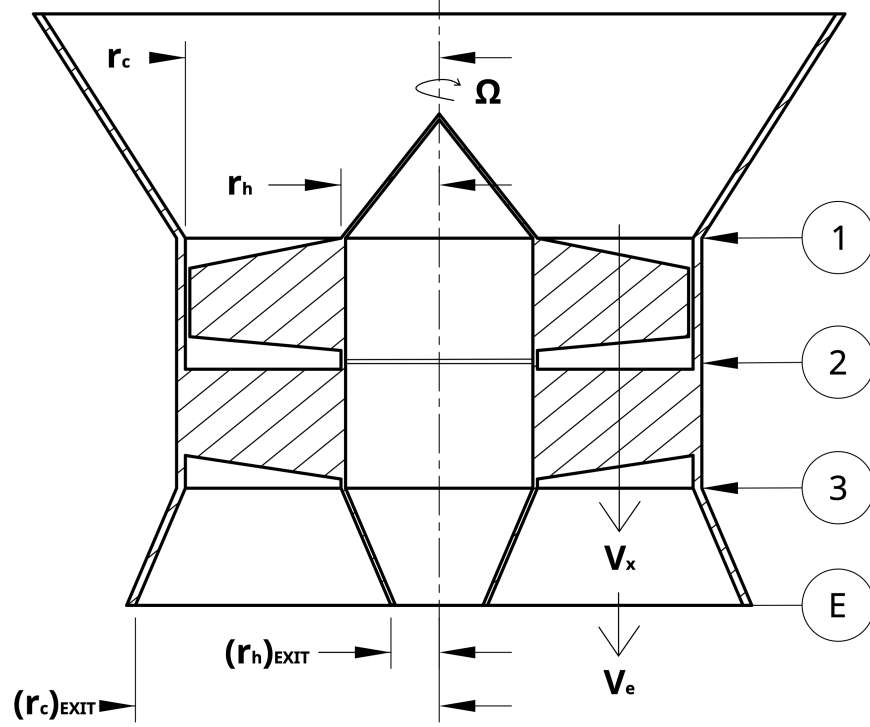


Figure 4: Configuration of ducted fan. **1**: Inlet plane; **2**: Inter-rotor-stator plane; **3**: Stator exit plane; **E**: Diffuser exit plane.

addition of a diffuser to reduce exit velocity – increasing efficiency – does not come at the cost of drag.

**Figure of Merit:**<sup>2</sup> The effectiveness of a propulsor in hover can be measured by the figure of merit,  $M_F$ , defined as a non-dimensional thrust-to-power ratio (Eqn. 2).

$$M_F = \frac{T}{P} \sqrt{\frac{T}{2\rho A_x}} \quad (2)$$

Considering a large control volume ( $V_{in} \approx 0$ ) around a simple ducted fan, treating the blade plane as a stagnation pressure actuator disk and the exit static pressure as atmospheric allows the theoretical thrust to be determined. This can then be written in terms of the blade passage quantities ( $A_x$ ,  $V_x$  etc) and the area ratio,  $\sigma$ , using continuity.

$$T = \dot{m}V_e = \rho A_e V_e^2 \quad \text{by continuity...} \quad \therefore T = \frac{\rho A_x V_x^2}{\sigma} \quad (3)$$

Theoretical power requirement can be determined by the rate of transfer of kinetic energy to the flow.

---

<sup>2</sup>REFERENCE PERIERA

$$P = \frac{1}{2}\dot{m}V_e^2 \quad \text{by continuity...} \quad \therefore P = \frac{\rho A_x V_x^3}{2\sigma^2} \quad (4)$$

Substituting Eqn. 3 and Eqn. 4 into Eqn. 2 gives the result in Eqn. 5.

$$M_F = \sqrt{2\sigma} \quad (5)$$

Hence to maximise hover performance the area ratio must be maximised. This necessitates a high performing diffuser with a minimised mass. Due to the negative effects of an adverse pressure gradient on flow attachment (and effective flow area) in a diffuser, the required length of a diffuser flow that remains attached will increase non-linearly with area ratio<sup>3</sup>. This trade-off between performance and weight limits the design choice of area ratio to avoid prohibitively heavy propulsors. Section 2.2.2 discusses this problem. This result also shows that a area ratio of 1, that is to say with no diffusion downstream of the blades, the theoretical figure of merit is  $M_F = \sqrt{2} \approx 1.414$ . Periera 2008<sup>4</sup> shows the maximum theoretical figure of merit for a propeller to be 1, therefore provided the area ratio remains above 0.5, fan figure of merit should be great than propeller performance in hover.

**Non-dimensional Operating Point:** The design of both the rotor and stator fan blades can be determined by the choice of non-dimensional operating point given by flow coefficient (Eqn. 6(a)) and stage loading (Eqn. 6(b)) where the mid-line blade velocity is  $U = \Omega \cdot r_m$  with  $r_m$  equal to the mid-line radius.

$$\phi = \frac{V_x}{U} \quad (a) \quad \psi = \frac{\Delta h_0}{U^2} \quad (b) \quad (6)$$

Assuming isentropic flow, stage loading can be written in terms of the stagnation pressure rise,  $\Delta p_0$ . Using Bernoulli and assuming exit static pressure is equal to atmospheric therefore gives an expression for  $\Delta h_0$  in terms of the exit velocity  $V_e$ .

$$\begin{aligned} \Delta p_0 &= (p_0)_e - (p_0)_{in} = (p_e + \frac{1}{2}\rho V_e^2) - p_a \\ \Delta p_0 &= \frac{1}{2}\rho V_e^2 \\ \therefore \Delta h_0 &= \frac{\Delta p_0}{\rho} = \frac{1}{2}V_e^2 = \frac{V_x^2}{2\sigma^2} \end{aligned} \quad (7)$$

Therefore  $\phi$ ,  $\psi$ , and  $\sigma$  are determined by Eqn. 8

$$\sigma^2 = \frac{\phi^2}{2\psi} \quad (8)$$

---

<sup>3</sup>REFERENCE ESDU

<sup>4</sup>REFERENCE PERIERA

The choice of operating point therefore sets the area ratio and consequently the theoretical figure of merit of the propulsor. Section 2.2.2 considers the interaction between the operating point and geometric variables, and the subsequent impact of required performance, whilst section 2.2.3 considers the embodiment of the design point into 3D rotor and stator blades.

**Estimation of Operating Fan Speed:** Equation 5 shows the effectiveness of a ducted fan in hover is independent of the speed of rotation of the fan. The fan speed however does impact the magnitude of the thrust developed, shown by substituting Eqn. 6(a) into Eqn. 3.

$$T = \frac{\rho A_x (\Omega r_m \phi_m)^2}{\sigma} \quad (9)$$

Equation 9 shows thrust to vary with both fan speed and fan size, and so the required thrust will vary depending on the choice of these parameters. The effect of fan size is discussed in section 2.2.2.

\*\*\*\*\*NOTES ON SECTION\*\*\*\*\*  
ESDU diffusion tables?

## 2.2.2 Mid-line Blade Design

**Mid-line Location:** Maximising the flow area for a given propulsor radius ensures minimum use of material and therefore a lighter design. This results in a small hub radius (20mm) and consequently very low hub-to-tip ratios compared to conventional compressors. As a result, selecting a mid-line at the mean radius introduces large differences in mass flow above and below the mid-line. This results in large variations in loading across the span. The alternative mid-line location is based on balancing the mass flow above and below the mid-line. This sets the mid-line radius at the root-mean-square off the hub and tip radii, as in Eqn. 10.

$$r_m = \sqrt{\frac{r_h^2 + r_c^2}{2}} \quad (10)$$

**Overall Performance:** As shown in section 2.2.1 the overall characteristics such as thrust and power can be determined from the fan geometry and the mid-line non-dimensional quantities  $\phi_m$  and  $\psi_m$ . Equation 5 suggested a larger area ratio will increase performance, however due to the difficulty of diffusing flow, the length of the diffuser required to enable large area ratios can be prohibitive. Further, on transition from static hover to horizontal flight a long diffuser will generate considerable drag due to its large flow facing area. A problem therefore arises when determining the required thrust. For steady hover, thrust must equal the weight of the vehicle. However as the design thrust varies, as does the

weight, creating a circular problem. In order to solve this a mass model is required that, given the propulsors operating point, estimates it's weight.

The variables required to define both the weight and performance of a ducted fan are outlined in table 1.

Table 1: Variables defining propulsor weight and performance

$r_c$	Blade passage casing radius
$r_h$	Blade passage hub radius
$\Omega$	Rotor angular velocity
$\sigma$	Diffusion factor
$\phi_m$	Mid-line flow coefficient
$\psi_m$	Mid-line stage loading

A notable exclusion from this list is the length of the diffuser, however the lower limit of this value is estimated from ESDU 75026:Figure 3<sup>5</sup> which gives empirical limits of diffuser lengths for symmetric annular diffusers. Therefore the length of the diffuser is determined by correlating the appropriate values from  $r_c$ ,  $r_h$ , and  $\sigma$  to the ESDU data.

Equations 3 and 4 can be expressed in terms of the variables in tab. 1 as follows

$$T = \frac{\rho\pi\phi_m^2\Omega^2(r_c^4 - r_h^4)}{2\sigma} \quad (11)$$

$$P = \rho\pi\phi\psi\Omega^3(r_c^2 - r_h^2)\left(\frac{r_c^2 + r_h^2}{2}\right)^{\frac{3}{2}} \quad (12)$$

Equation 11 can be equated to the vehicle weight to determined the variables required for hover. A mass model is developed to enable this.

**ESDU 75026 Diffuser Data:** ESDU 75026 presents the performance of circular annular diffusers in incompressible flow.

$$C_{pr} = \frac{p_e - p_x}{\frac{1}{2}\rho V_x^2} \quad (13)$$

ESDU 75026:Figure 3 shows the line of  $C_{pr}^{**}$  representing the length ratio at which  $C_{pr}$  (Eqn. 13) is maximised for a given area ratio. This allows a minimum diffuser length to be determined for a given area ratio and upstream span ( $r_c - r_h$ ). This line can be approximated with an R-squared value of 0.9999 by

$$\frac{L}{r_c - r_h} = -5.56\sigma^3 + 24.16\sigma^2 - 23.41\sigma + 5.413 \quad (14)$$

---

<sup>5</sup>REFERENCE ESDU TABLES HERE

**Mass Model – Diffuser:** The diffuser hub and casing are modelled as a hollow truncated cone 3D printed in PLA with height  $L$  (determined by Eqn. 14), a base radius  $r_h$  (for the hub) and  $(r_c)_{EXIT}$  (for the casing), a truncation radius of  $(r_h)_{EXIT}$  (for the hub) and  $r_c$  for the casing, and a thickness  $t$ , as in Fig. 6. Equation 15 gives the volume of a hollow truncated cone with the respective values of  $R$ ,  $r$ ,  $S$ , and  $s$  for the hub and casing defined in tab. 2.

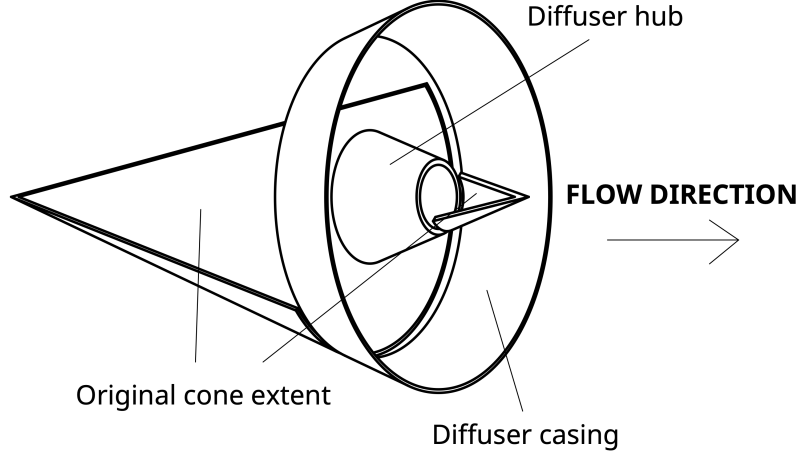


Figure 5: Hollow truncated cone diffuser model showing original extent of cone before truncation

	Hub value	Casing value
<b>R</b>	$r_h$	$(r_c)_{EXIT} + t$
<b>r</b>	$(r_h)_{EXIT}$	$r_c + t$
<b>S</b>	$r_h - t$	$(r_c)_{EXIT}$
<b>s</b>	$(r_h)_{EXIT} - t$	$r_c$
<b>h</b>	$L$	$L$

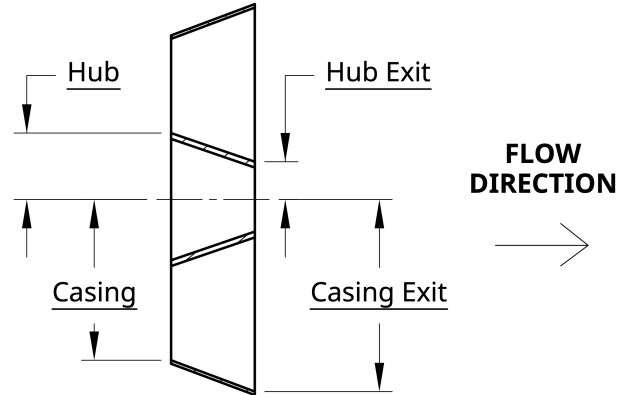


Figure 6: Dimensions of hollow truncated cone diffuser model

Table 2: Parameter values for diffuser hub and casing

$$V = \frac{h\pi}{3}(R^2 + Rr + r^2 - S^2 - Ss - s^2) \quad (15)$$

$$m_{DIFF.} = \rho_{PLA}(V_{HUB} + V_{CASE}) \quad (16)$$

From the ESDU data, a annulus flow with uniform axial velocity is diffused in the shortest distance if the diffuser is symmetric such that the diffuser angle at casing and hub is equal giving

$$\frac{(r_c)_{EXIT} - r_c}{L} = \frac{r_h - (r_h)_{EXIT}}{L} \quad (17)$$

Applying Eqn. 17 and expanding Eqn. 1 in terms of radius, the diffuser exit hub and casing radii can be determined.

$$(r_h)_{EXIT} = \frac{r_c + r_h}{2} - \frac{\sigma}{2}(r_c - r_h) \quad (18)$$

$$(r_c)_{EXIT} = \frac{r_c + r_h}{2} + \frac{\sigma}{2}(r_c - r_h) \quad (19)$$

Substituting Eqn. 18 and Eqn. 19 into Eqn. 15, Eqn. 16 can be solved to approximate the mass and therefore the weight of a diffuser at a particular set of design parameters.

**Mass Model – Blade Passage:** The blade passage (excluding rotor and stator) are modelled as a straight annulus 3D printed in PLA. The passage itself has inner radius  $r_h$  and outer radius  $r_c$ . The casing is modelled to have thickness of  $t_c = 1.5mm$  and the hub section has a thickness of  $t_h = 5mm$ . The length of the blade passage is  $L_{BP} = 70mm$  giving a volume of

$$V_{BP} = L_{BP}\pi[2r_h t_h - t_h^2 + 2r_c t_c + t_c^2] \quad (20)$$

Multiplying by the density of PLA gives the mass of the blade passage section, which can be written in terms of the unknown variable  $r_c$  and  $r_h$

$$m_{BP} = 2.73r_h + 0.818r_c - 0.0062 \quad (21)$$

**Mass Model – Intake:** For simplicity the intake is also modelled as a hollow truncated cone, an approximation for it's actual ellipsoidal geometry. It has approximately equal length to it's change in radius which is set approximately equal to the blade passage span,  $r_c - r_h$ . Therefore using Eqn. 15, and assuming a thickness of  $1mm$ , the intake mass can be approximated by

$$m_{IN.} = 3.90(r_c - r_h)(3r_c - r_h + 0.001) \quad (22)$$

**Mass Model – Blades:** As the number of blades has not yet been determined, the blades are modelled as having the equivalent mass of a annular flat disk of thickness  $t_{ROTOR} = 1.5mm$  for the rotor and  $t_{STATOR} = 3mm$  for the stator. The resulting mass is given by

$$V_{BLADES} = \pi(r_c^2 - r_h^2)(t_{ROTOR} + t_{STATOR}) \quad (23)$$

$$m_{BLADES} = 17.5(r_c^2 - r_h^2) \quad (24)$$

**Thrust = Weight:** The mass model described above provides an approximation for the mass of a particular design based on the design parameters listed in tab. 1. In hover, the load carried by each propulsor is equal to the propulsor's weight and its share of the payload weight (4 propulsors). The payload here is the flying test bed chassis and battery, described in section 2.1.1. Using Eqn. 11 the thrust developed can be set equal to the required thrust to give the relationship between the design variables when the propulsor is operating in the static hover state.

$$T = g \left[ m_{PROPULSOR} + \frac{m_{CHASSIS}}{4} + \frac{m_{BATTERY}}{4} \right] \quad (25)$$

$$\frac{\rho \pi \phi_m^2 \Omega^2 (r_c^4 - r_h^4)}{2\sigma} = g[m_{DIFF.} + m_{BP} + m_{IN.} + m_{BLADES}] + 2.44N \quad (26)$$

**Reduction of Unknown Variables:** In order to solve the design problem, the number of unknowns must be reduced. This is achieved by fixing the propulsor size. The application demonstrated here is for a small quad-copter style vehicle. Furthering work carried out by Jonny 2019<sup>6</sup> in which the performance of a ducted fan was determined with  $M_F > 1$  and  $r_c = 120mm$ , this design is to be scaled by a half giving

$$r_c = 60mm \quad (27)$$

The value of  $r_h$  is determined by the outer diameter of the electric motor used to drive the rotor. This is typically  $d < 35mm$ , therefore  $r_h$  is chosen to be

$$r_h = 20mm \quad (28)$$

Giving a hub-to-tip ratio of 0.333. This leaves area ratio,  $\sigma$ , and the rotor angular velocity,  $\Omega$ . The relationship between the design parameters  $\phi$ ,  $\psi$ , and  $\sigma$ , as well as the relationship between diffuser length and  $\sigma$ , results in a limit on the design point due to the requirement for diffuser length,  $L_{DIFF.}$ , to not become prohibitive (as discussed in sec. 2.2.2: *Overall Performance*). This is limited to  $L_{DIFF.} \leq 100mm$ . Therefore from Eqn. 14

---

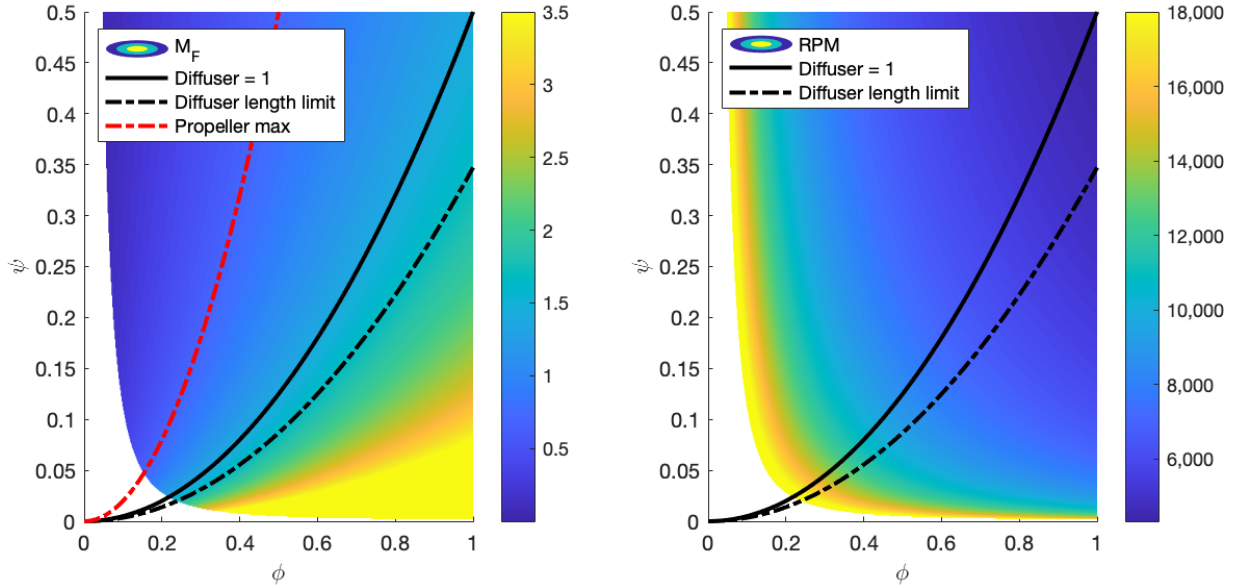
<sup>6</sup>CUED 4th Year Project Report June 2019



$$-5.56\sigma^3 + 24.16\sigma^2 - 23.41\sigma + 5.413 \leq 2.5 \quad (29)$$

$$\therefore \sigma \leq 1.2 \quad (30)$$

It should be noted that this limit on  $\sigma$  arises from the performance of a conventional circular annular diffuser, as presented in ESDU 75026. This limit may be exceeded however through the use of various flow devices, such as splitter vanes. These ideas are discussed further in the future work section (sec. 5) and are not implemented here. With the other parameters set, the thrust = weight condition sets the value of  $\Omega$  at each design point. The required motor speed impacts the choice of electric motor used as the maximum efficiency range will vary.



(a) Figure of merit as a function of  $\phi$  and  $\psi$  (b) Motor speed in RPM as a function of  $\phi$  and  $\psi$  satisfying hover condition of thrust = weight

Figure 7: Contour plots of the  $\phi$ - $\psi$  design space generated using mass model. Plots display the diffuser limit arising from a maximum diffuser length, and the line representing a area ratio of 1.

Figure 7a shows the variation in figure of merit across the design space. The diffuser length limit considerably constrains what sections of the design space are accessible, regardless the majority of the design space provides significantly better hover performance than a propeller. Figure 7b shows the variation in required motor speed (in RPM) across the design space. The required optimum efficiency range for the electric motor must be between 5,500 – 14,000 RPM. In order to reduce motor size the lower end of this range is chosen

Table 3: Propulsor design point

$r_c$	60mm
$r_h$	20mm
$r_m$	44.7mm (RMS)
$\Omega$	6230 RPM
$\sigma$	1.1314
$L_{DIFF}$	72.0mm
$\phi_m$	0.80
$\psi_m$	0.25

(this is discussed in more detail in Section 2.3) therefore  $\Omega \sim 6500$  RPM. SOMEONE 20XX<sup>7</sup> shows suitable range for flow coefficient in incompressible turbomachinery to not exceed 0.8, and stage loading to not exceed 0.3. Considering Fig. 7b a line of constant RPM at approximately 6500 RPM in the region between the two diffuser limits passes from top-left to bottom-right. Figure 7a shows figure of merit to increase towards the bottom-right and so to satisfy all the conditions above and maximise figure of merit, an operating point is chosen with  $\phi_m = 0.8$  and  $\psi_m = 0.25$  and is tabulated in Table 3.

Conventional propulsive turbomachines, such as high bypass ratio turbo-fans must limit their flow coefficient as this comes at the cost of propulsive efficiency. The propulsor considered here however differs from this as it diffuses the exit flow, reducing it's velocity and therefore reducing exit loss.

**Velocity Triangles:** Now the design parameters have been determined the mid-line velocity triangles can be drawn for this particular design.<sup>8</sup> Figure 8 shows the velocity triangles in context with rotor and stator blades. Flow angles are measured positive in the sense of rotor rotation (in Fig. 8 positive down).

### 2.2.3 3D Blade Design

Overall performance has been determined by setting the mid-line values of flow coefficient,  $\phi_m$ , and stage loading,  $\psi_m$ . The values of  $\phi$  and  $\psi$  must vary along the span as the local value of blade speed changes, and for equilibrium to be maintained across the flow passage. In order to satisfy these conditions the radial equilibrium equation must be satisfied. Potential solutions to this equation are discussed below.

**3-dimensional Flow Solutions to Radial Equilibrium:** Radial equilibrium states that for axi-symmetric and incompressible annulus flow Eqn. 31 must be satisfied.

<sup>7</sup>REFERENCE SMITH CHARTS? LOOK AT WHY LIMITING PSI and PHI

<sup>8</sup>PUT DERIVATION OF TRIANGLE ANGLES IN APPENDIX?

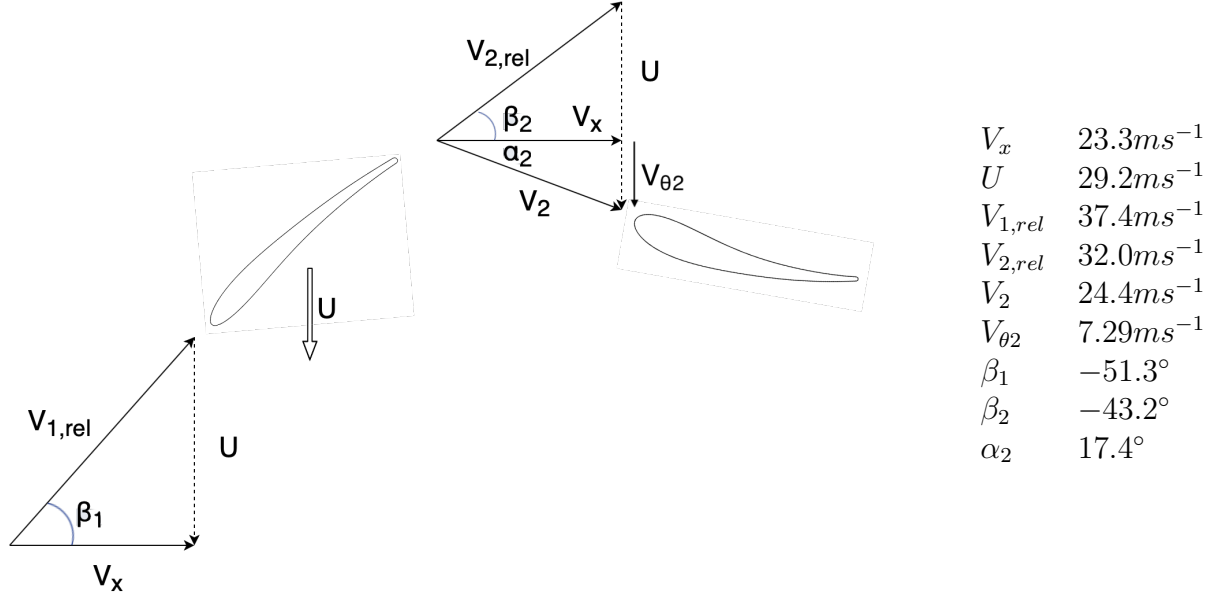


Figure 8: Mid-line velocity triangles (stator exit omitted as flow axial at exit)

$$\frac{dh_0}{dr} - T \frac{ds}{dr} = V_x \frac{dV_x}{dr} + \frac{V_\theta}{r} \frac{d(rV_\theta)}{dr} \quad (31)$$

Assuming there is no variation in stagnation enthalpy or entropy across the span, this reduces to

$$V_x \frac{dV_x}{dr} + \frac{V_\theta}{r} \frac{d(rV_\theta)}{dr} = 0 \quad (32)$$

Noting Eqn. 6 and applying Euler's work equation, we obtain

$$\phi r \frac{d(\phi r)}{dr} + \psi \frac{d(\psi r^2)}{dr} = 0 \quad (33)$$

Which has general solutions in the form

$$\phi = \phi_m \left( \frac{r}{r_m} \right)^A \quad (a) \quad \psi = \psi_m \left( \frac{r}{r_m} \right)^B \quad (b) \quad (34)$$

Where  $\phi_m$  and  $\psi_m$  are the mid-line quantities. Substituting eqns.34a & 34b into Eqn. 33 gives<sup>9</sup>

$$\left[ \phi_m \left( \frac{r}{r_m} \right)^A \right]^2 (1 + A) = - \left[ \psi_m \left( \frac{r}{r_m} \right)^B \right]^2 (2 + B)$$

---

<sup>9</sup>STICK THE DERIVATION IN AN APPENDIX???

$$\therefore \phi^2(1 + A) = -\psi^2(2 + B) \quad (35)$$

This solution can be used to determine the values of the exponents,  $A$  and  $B$ . The constant  $B$  is referred to here as the vortex distribution exponent as it determines the tangential velocity variation in the  $r$ - $\theta$  plane.

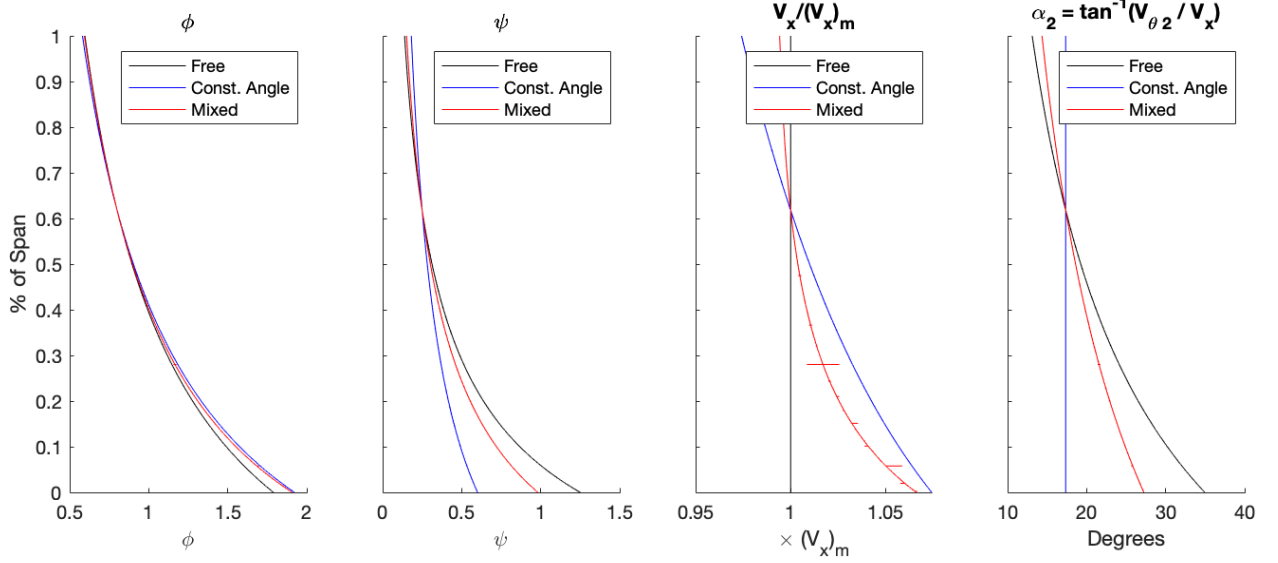


Figure 9: Distributions of design parameters  $\phi$  and  $\psi$  and non-dimensionalised axial and tangential velocities,  $V_x$  and  $V_{\theta 2}$  respectively, across the span at 3 different boundary conditions (free vortex, constant angle and mixed vortex).

**Free Vortex ( $B = -2$ ):** One such distribution arises from the free vortex condition. This results from the solution to Eqn. 35 in which both LHS and RHS are equal to zero giving

$$A = -1 \quad (a) \qquad B = -2 \quad (b) \quad (36)$$

Therefore from Eqn. 34a and Eqn. 36a

$$\phi(r) \sim \frac{1}{r} \qquad \therefore \frac{d}{dr}(V_x) = 0 \quad (37)$$

Therefore axial velocity across the span must be constant. Similarly it can be shown from Eqn. 34b and Eqn. 36b

$$\psi(r) \sim \frac{1}{r^2} \qquad \therefore \frac{d}{dr}(\Delta h_0) = 0 \quad (38)$$

Therefore the loading is equal across the span. It can then be determined that  $V_{\theta 2} \sim 1/r$

resulting in a vorticity free (lowest loss) flow<sup>10</sup>. Both the constant  $V_x$  and the constant  $\Delta h_0$  conditions indicate uniform exit static pressure. In practice the variation in  $V_{\theta 2}$  across the span results in large variations in blade twist angle that can reduce efficiency (see Fig. 9 that shows  $V_{\theta 2}$  variation resulting in over  $20^\circ$  of absolute flow angle variation).<sup>11</sup>

Furthermore, Fig. 9 shows stage loading,  $\psi$ , to become larger than 1 at radii close to the hub. From Euler, and given axial inlet flow

$$\Delta V_\theta = V_{\theta 2} = \psi U \quad (39)$$

This shows the tangential velocity at the hub to be greater than the local blade speed. By reducing the value of the vortex distribution exponent,  $B$ , this can be avoided by keeping  $\psi \leq 1$ .

**Mixed Vortex** ( $-2 \leq B \leq 0$ ): Equation 35 can also be used to numerically solve the radial equilibrium equation for any value of the vortex distribution exponent provided  $\phi_m$  and  $\psi_m$  are known. A summary of vortex distribution exponent values is shown in tab. 4. The mixed vortex design shown in Fig. 9 has a vortex distribution exponent of  $-1.7$ . This produces a vortex distribution that, at the hub, has a tangential velocity is equal to the velocity of the hub wall. This reduces the absolute velocity of the flow past the wall and therefore minimises frictional loss at the hub. Hereafter any reference to a ‘mixed vortex condition’ corresponds to a vortex distribution exponent of  $B = -1.7$ , as described here.

**Constant Angle:** Another common design is for constant absolute flow angle across the span, such that

$$\frac{d}{dr} \left( \frac{V_\theta}{V_x} \right) = 0 \quad (40)$$

$$\therefore \frac{\psi}{\phi} = \text{constant} \left( = \frac{\psi_m}{\phi_m} \right) \quad (41)$$

This results in the exponents A and B being equal giving

$$A = B = - \left( \frac{2\psi_m^2 + \phi_m^2}{\psi_m^2 + \phi_m^2} \right) \quad (42)$$

**3D Velocity Triangles:** Once the distributions of  $\phi$  and  $\psi$  have been determined the variation in flow velocities and angles can be found across the span. The value of any velocity or angle can be found using the appropriate local values of the spanwise variables  $\phi$ ,  $\psi$ ,  $U$ , and  $r$ . The relative merits of each of the vortex distributions are discussed in Section 4.1.1

<sup>10</sup>REFERENCE DIXON AND HALL FLUID MECHANICS AND THERMODYNAMICS OF TURBO-MACHINERY, CHAPTER 6.3, P218

<sup>11</sup>AGAIN NEED A REFERENCE FOR THIS?

Table 4: Vortex distribution exponents for various boundary conditions

	Free Vortex $V_x(r) = \text{const.}$	Constant Angle $V_x/V_\theta = \text{const.}$	$B = \dots$ see Eqn. 35
<b>A</b>	-1	$-\left(\frac{2\psi_m^2 + \phi_m^2}{\psi_m^2 + \phi_m^2}\right)$	<i>Solve numerically</i>
<b>B</b>	-2	$-\left(\frac{2\psi_m^2 + \phi_m^2}{\psi_m^2 + \phi_m^2}\right)$	<i>Solve numerically</i>

in which the three designs presented here are tested.

**Validation of Mid-line Location:** Eqn. 11 and Eqn. 12 come from the assumption that mid-line design parameters are representative of the performance of the whole flow. This assumption can be verified now that the span-wise distributions of the flow parameters has been determined. Integrating the work done and thrust generated by an infinitesimal annulus element allows the real power and thrust produced by the propulsor to be determined. This is computed numerically using 99999 elements and the expression obtained above for each of the parameters in Eqn. 45.

$$P = \int \Delta h_0 \cdot d\dot{m} \quad (43)$$

$$\Delta h_0 = \psi U^2 \quad (a) \quad d\dot{m} = \rho V_x (2\pi r dr) \quad (b) \quad (44)$$

$$\therefore P = 2\pi\rho\Omega^3 \cdot \frac{\phi_m\psi_m}{r_m^{B+A}} \int_{r_h}^{r_c} r^{A+B+3} dr \quad (45)$$

A similar expression can be obtained for the thrust developed. The mass-averaged mid-line radius definition of  $r_m$  is compared to the conventional mean-line radius definition of  $r_m$  in Table 5 by calculating the error between the real power and thrust and the predicted one obtained from Eqn. 12 and Eqn. 11. A properly balance mid-line radius choice will ensure the real power is as close to the predicted one as possible, minimising this error

Table 5 clearly shows the selection of a mid-line radius at the RMS of the hub and casing radius reduces the error between the real and the predicted power requirements considerably. These errors are small enough to be neglected and so this choice of mid-line radius is validated.

Table 5: Comparison of power requirement from predicted (from constant mid-line parameters) and real (from integral of span-wise distributions) using various mid-line locations. A mixed vortex design is used though the behaviour is also displayed in other all other vortex designs

Mid-line radius	$P$ error	$T$ error
$r_m = \text{mean}(r_c, r_h)$	37%	24%
$r_m = \text{RMS}(r_c, r_h)$	1.2%	0.36%

**Blade Number and Span-wise Chord:** Lieblein, Schwenk and Broderick (1953)[?] present a correlation for diffusion factor as a function of velocities and the pitch-chord ratio of the blades.

$$DF = \left(1 - \frac{V_{2,rel}}{V_{1,rel}}\right) + \left(\frac{V_{\theta 1,rel} - V_{\theta 2,rel}}{2V_{1,rel}}\right) \frac{s}{c} \quad (46)$$

Given that the change in tangential flow velocity is the same in both the absolute and the rotor relative reference frames, and the inlet flow is axial, this becomes

$$DF = \left(1 - \frac{V_{2,rel}}{V_{1,rel}}\right) + \left(\frac{V_{\theta 2}}{2V_{1,rel}}\right) \frac{s}{c} \quad (47)$$

This expression is valid for both the rotor and stator provided the relative values are taken in the respective blade's frame off reference.

Having determined the span-wise variation in the flow velocities and angles in Section 3*D Velocity Triangle* above, the value of the local pitch-chord ratio,  $s/c$ , can be found provided a suitable diffusion factor is chosen. Consider first a constant value of diffusion factor that lies below the separation limit,  $DF = 0.6$ , such as  $DF = 0.45$ . Pitch-chord across the span can be determined as

$$\frac{s}{c} = \left[ DF - \left(1 - \frac{V_{2,rel}}{V_{1,rel}}\right) \right] \left( \frac{2V_{1,rel}}{V_{\theta 2}} \right) \quad (48)$$

In order to determine span-wise pitch, the number of blades must be determined using the mid-line values. The mid-line chord is estimated using the blade mid-line aspect ratio where  $AR = \text{span}/\text{chord} = l/c$

$$c_m = \frac{r_c - r_h}{AR} \quad (49)$$

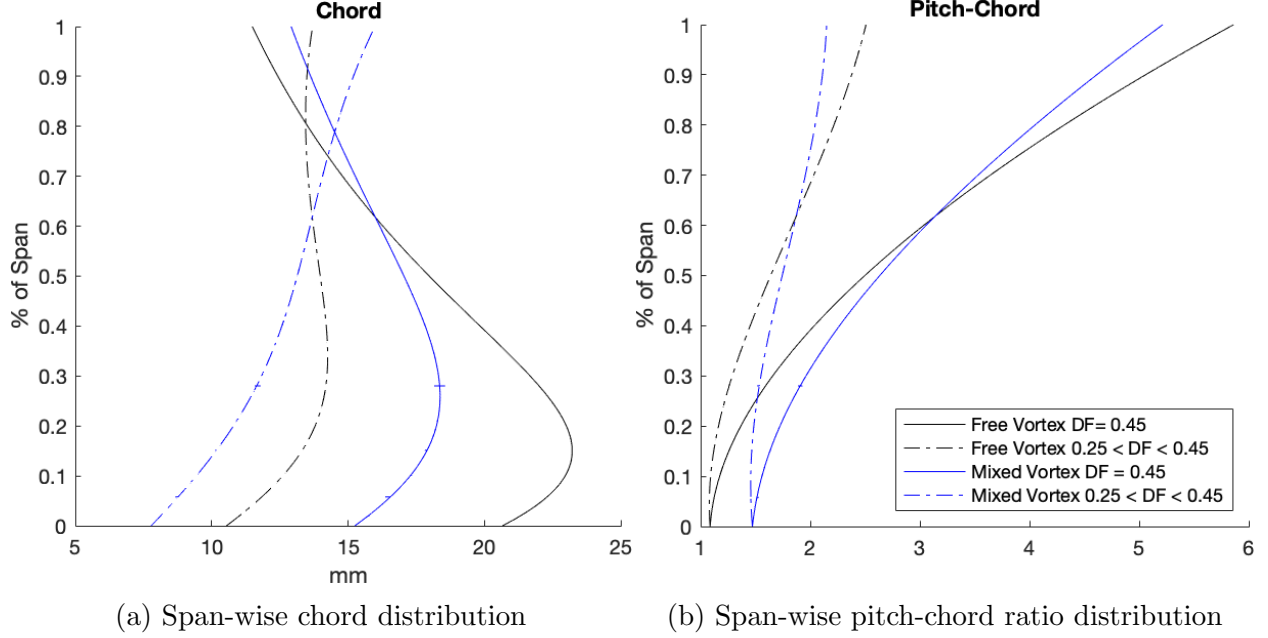


Figure 10: Span-wise distributions are shown for both the free and mixed vortex conditions (black and blue lines respectively). Each is also shown with a constant value of diffusion factor ( $DF = 0.45$ , solid line) and varying diffusion factor linearly across the span ( $DF_{HUB} = 0.45$ ;  $DF_{TIP} = 0.25$ , dot-dashed line)

$$N = \frac{2\pi r_m}{(s/c)_m c_m} \quad (50)$$

The blade number is rounded up to the next integer value. Care must be taken when selecting the blade numbers of the rotor and stator. Lower common multiples of blade number will result in more blade interaction and therefore higher acoustic dB. If possible, odd or prime numbers are selected to minimise interaction, provided this number is not too far from the calculated value. Table 6 at the end of this section (*Blade Number and Span-wise Chord*) outlines the calculated and selected blade numbers for each of the designs discussed. Using the blade number the local chord can be determined using local pitch-chord ratio and radius such that

$$c = \frac{2\pi r}{(s/c)N} \quad (51)$$

The resulting span-wise chord distribution from both the free and mixed vortex conditions are shown in Fig. 10a (solid line). For the free vortex condition it shows the variation in chord across the span to be large with the tip chord is less than half the maximum chord. Changing to the mixed vortex condition reduces this variation significantly with both the tip chord increasing and the hub chord decreasing. This variation arises from Eqn. 48 as the range of velocities across the span, and the constant diffusion factor, result in large variations



in pitch-chord ratio (as in Fig. 10b).

Lieblein (1953) shows the increase in loss for diffusion factors above 0.55 in the hub to mid-line regions, and 0.3 in the tip region. Therefore it would be beneficial to vary the design diffusion factor across the span to avoid these values whilst maintaining as high a loading as possible. The dot-dashed lines in Fig. 10b show the same operating point as the solid lines but with the diffusion factor varying linearly from 0.45 at the hub to 0.25 at the tip. The resulting distribution of pitch-chord is much flatter. In the case of the free vortex condition this results in an almost uniform chord profile.

Table 6: Blade numbers at various design conditions

Vortex Design	Diffusion Factor	N	N (selected)
Free Vortex	$DF = 0.45$	5.60	6
	$0.25 \leq DF \leq 0.45$	5.60	6
Mixed Vortex	$DF = 0.45$	10.97	11
	$0.25 \leq DF \leq 0.45$	10.97	11

Consistency in pitch-chord has further implications for deviation and is explored in the following section.

**Deviation:** Deviation in flow angle from the blade metal angles is estimated from correlations proposed by Howell (1945)[?], (1945)[?], and Carter (1950)[?], commonly referred to as Carter’s rule states for a compressor blade

$$\delta = m\theta\sqrt{\frac{s}{c}} \quad (52)$$

Where  $\theta$  is the flow turning achieved in the relative frame, and  $m$  is an empirically determined variable that can be approximated by

$$m = 0.23\left(\frac{2a}{l}\right)^2 + \frac{\beta_2}{500} \quad (53)$$

Where for a circular arc camber line  $a/l = 0.5$ . Hence the deviation varies  $\sim \sqrt{s/c}$ . Figure 11a shows the large increase in deviation angle at the blade tips for both the free and the

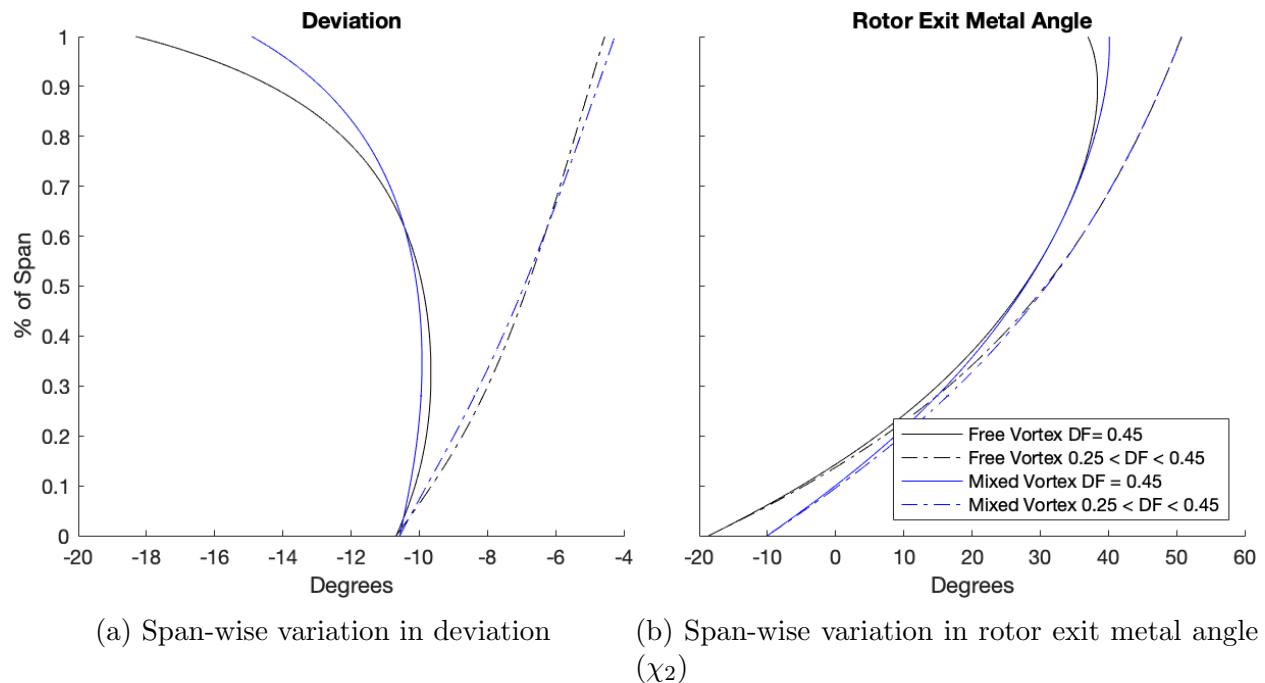


Figure 11: Span-wise distributions are shown for both the free and mixed vortex conditions (black and blue lines respectively). Each is also shown with a constant value of diffusion factor ( $DF = 0.45$ , solid line) and varying diffusion factor linearly across the span ( $DF_{HUB} = 0.45$ ;  $DF_{TIP} = 0.25$ , dot-dashed line)

mixed vortex conditions when a constant diffusion factor is used (solid lines). Introducing a varying diffusion factor (dot-dashed lines) across the span greatly reduces this deviation due to the fact the loading is now spread over a larger chord. Carter's rule is derived from empirical results obtained from compressor cascades, and as such it is not suitable to apply it to blades with large span-wise variations in pitch-chord ratio. By applying a varying diffusion factor the range of pitch-chord ratio reduces significantly and Carter's rule produces more reliable results. Consequently the variation in rotor exit metal angle is more consistent and contains no mid-span maxima, as in Fig. 11b.

\*\*\*\*\* NOTES \*\*\*\*\*

- Fixed deviation design?

### Blade Sweep and Lean: Sweep/Lean

- Reference JVT
- Obtuse angles at tip and hub
- Sweep to reduce size of design

### Blade Profiles: Profiles

- Where did they come from?

- What are they?
- How are they implemented?

**Notes on Design Code:** Blade design code

- How does all this fit together?

## 2.3 Electrical Design

With the propulsor design specified the electrical design must be considered to provide the correct power to drive the propulsors. The electric motor and corresponding power supply is chosen to be compatible with both the propulsor aerodynamic design and the system control and instrumentation architecture.

### 2.3.1 Motor Requirements

In Section 2.2.2 the motor speed and design point (therefore the required shaft torque) is set. Required motor speed is found to be 6230 RPM. The theoretical torque required can be found by considering the power transferred to the flow and equating this to the shaft power (neglecting aerodynamic losses). From Eqn. 12 and defining shaft power  $P = T_s \cdot \Omega$

$$T_s = 0.094 Nm \quad (54)$$

### 2.3.2 Choice of Electric Motor

Size ( $d < 36mm$ )

### 2.3.3 Power Supply

Want to simulate using a battery pack for actual flight conditions but increase run-time. Choose 12V steady state operating voltage (14.8V nominal Li-Po).

### 2.3.4 Instrumentation Design

Maybe reference here but give details in the appendix? Described more in section 3.2.2 RPM

Thrust

- Calibration

Power

Pressures

## 2.4 Mechanical Design

The design of the rotor and stator of the propulsor has been completed with the 2D design parameters and velocity triangles specified in Table. 3 and Fig. 8 respectively, and the 3D blade parameters specified in Table: ???. Further, the electrical specifications have been set and the electric motor chosen. In this section the propulsor design is embodied and the mechanical aspects of the design considered.

### 2.4.1 Propulsor Dimensions

\*\*\*\*\* NOTES \*\*\*\*\*

- Overview of design
- Modular propulsor design, subcomponents

Thrust = Weight condition  
Mass model to close the problem

### 2.4.2 Shroud Tip Clearance

Shroud thickness  
FEA  
3D printer tolerances

### 2.4.3 Hollow Stators

Power supply  
Weight reduction  
Tolerance  
How to

### 2.4.4 3D Printing

Printer used  
Printer tolerance  
Design adjustments to enable good printing

- Straight TRAILING edge
- Raft and reduce air-gap

# Methods

## 3.1 Experiments

### 3.1.1 Stationary Propulsor Test

Setup

- Stand

Test variables

- Speeds

- Sigma

- Rotor design

### 3.1.2 Flying Test Bed

## 3.2 Experimental Method & Data Processing

### 3.2.1 Non-dimensional Quantities

Pressure quantities, FOM,  $\phi$ ,  $\psi$ .

### 3.2.2 Instrumentation

Power (DC Current and Voltage), Thrust, FOM, RPM, Pressures

### 3.2.3 Data Acquisition

Acquisition and integration of systems and software.

### 3.2.4 Flight Management for Auto Position Hold

System not used.

### 3.2.5 Cage Design & Tether

# Experimental Results

## 4.1 Stationary Propulsor Test

### 4.1.1 Comparison of Vortex Distributions

### 4.1.2 Version 1.0 EDF

Heavy Blue: 3 exits and 3 rotor vortex designs. Comparison of intake performance (long and short).

- Power (Current and Voltage)
- Thrust
- FOM
- RPM

#### **4.1.3 Version 2.0 EDF**

1 exit and 2 rotor vortex designs. Long intake only.

- Power (Current and Voltage)
- Thrust
- FOM
- RPM
- Pressures

#### **4.1.4 Version 3.0 EDF**

1 exit and 1 rotor vortex designs. Long intake only.

- Power (Current and Voltage)
- Thrust
- FOM
- RPM
- P1 Only

#### **4.1.5 Propeller**

### **4.2 Hover Tests**

#### **4.2.1 Propeller Performance**

#### **4.2.2 Hover Test Limitations**

## **Future Work**

Future work can be a proper section

Do the hover tests

Manoeuvre tests

- Look at what the  $M_f$  vs manoeuvre metric would look like
  - What could the manoeuvre metric look like?
- Actual theory on contra-rotating

## **5.1 Propulsor Design**

### **5.1.1 Stationary Propulsor Tests**

What else would I have done to finish these off?

### **5.1.2 Contra-rotating Ducted Fan**

Motivation for CR design More smaller motors better? CAD of what it might look like.  
Velocity triangles ie Do the design and see how it would work theoretically.

### **5.1.3 Computational Fluid Dynamics**

- Discuss limitations of design method (with respect to previous sections on deviation etc.
- Reference Megs work? Show that CFD can get close to experimental results ie prove the method.

## **5.2 Flying Test Bed Experiments**

How to quantify manoeuvre stability? The 'Eriksen' manoeuvre?

## **Conclusions**

## **Appendix A: COVID-19**

## **Appendix B: Derivations**

Velocity triangles?

## **Temporary Appendix Figures**

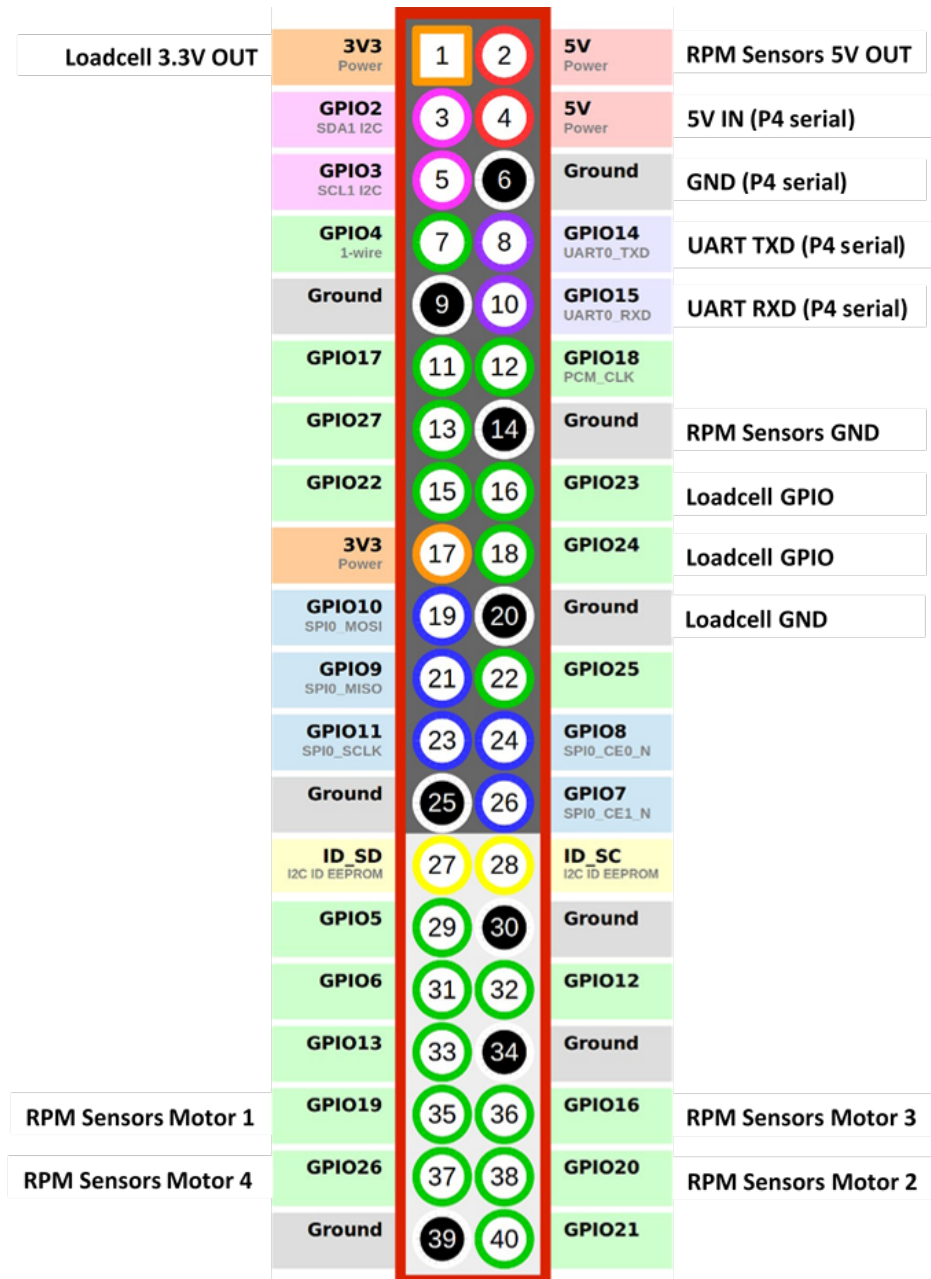


Figure 12: RPi3 header board with labelled used pins



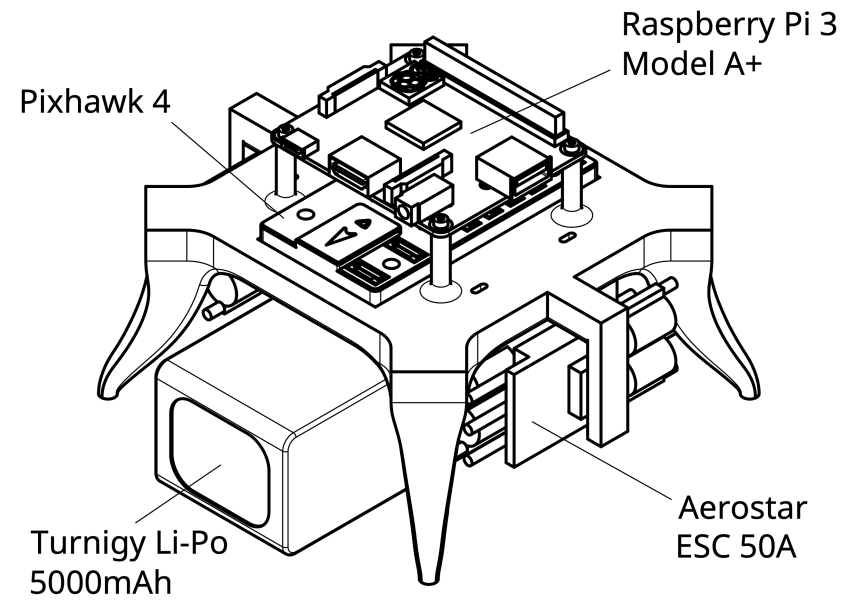
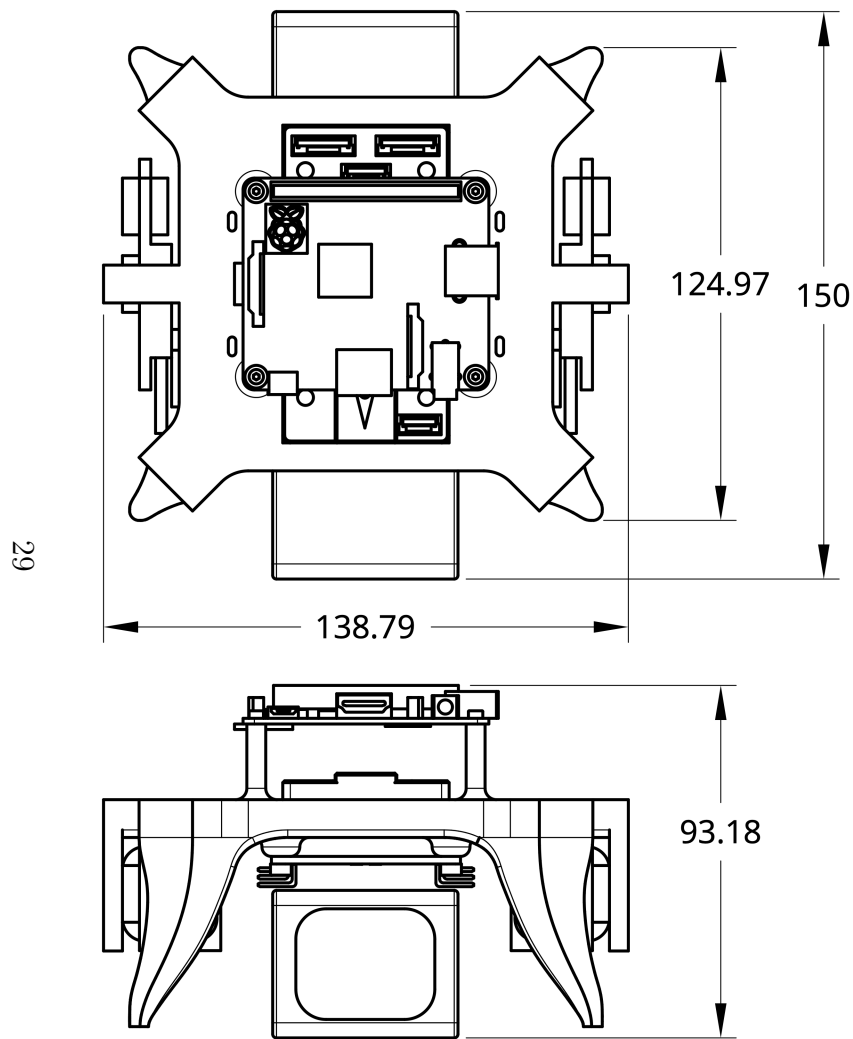


Figure 13: 3rd Angle projection of flying test bed chassis with principal dimensions and an isometric view